Structure
Article

The Cap-Binding Translation Initiation Factor, eIF4E, Binds a Pseudoknot in a Viral Cap-Independent Translation Element

Zhaohui Wang,[1,4] Marc Parisien,[2] Kay Scheets,[3] and W. Allen Miller[1,*]
[1]Plant Pathology Department, and Biochemistry, Biophysics, and Molecular Biology Department, Iowa State University, Ames, IA 50011, USA
[2]Department of Biochemistry and Molecular Biology, University of Chicago, Chicago, IL 60637, USA
[3]Department of Botany, Oklahoma State University, Stillwater, OK 74078, USA
[4]Current address: University of Texas Southwestern Medical Center, Dallas, TX 75390 USA
*Correspondence: wamiller@iastate.edu
DOI 10.1016/j.str.2011.03.013

SUMMARY

Eukaryotic initiation factor eIF4E performs a key early step in translation by specifically recognizing the m^{7}GpppN cap structure at the 5′ end of cellular mRNAs. Many viral mRNAs lack a 5′ cap and thus bypass eIF4E. In contrast, we reported a cap-independent translation element (PTE) in Pea enation mosaic virus RNA2 that binds and requires eIF4E for translation initiation. To understand how this uncapped RNA is bound tightly by eIF4E, we employ SHAPE probing, phylogenetic comparisons with new PTEs discovered in panico- and carmoviruses, footprinting of the eIF4E binding site, and 3D RNA modeling using NAST, MC-Fold, and MC-Sym to predict a compact, 3D structure of the RNA. We propose that the cap-binding pocket of eIF4E clamps around a pseudoknot, placing a highly SHAPE-reactive guanosine in the pocket in place of the normal m^{7}GpppN cap. This reveals a new mechanism of mRNA recognition by eIF4E.

INTRODUCTION

In the highly regulated first step in translation initiation, the m^{7}GpppN cap structure, present at the 5′ end of all nonviral eukaryotic mRNAs, recruits the ribosome via the eukaryotic initiation factor, eIF4F. In plants, eIF4F is a heterodimer of eIF4E and eIF4G (Browning, 2004). The eIF4G subunit of eIF4F binds simultaneously to eIF4E, poly(A)-bound poly(A) binding protein, and directly to the mRNA (Wells et al., 1998). This circularizes the mRNA and attracts eIF3 that docks the 43S ribosome preinitiation complex and associated initiation factors to the 5′ end of the mRNA (Jackson et al., 2010). The complex then scans in the 3′ direction in search of the initiation codon, usually AUG.

X-ray crystallography and NMR studies revealed that the cap binds eIF4E via π-π stacking between two tryptophan residues in a pocket in the concave surface of eIF4E (Marcotrigiano et al., 1997; Matsuo et al., 1997; Monzingo et al., 2007). The 7-methyl group introduces a positive charge that enhances the interaction with the electronegative π bonds. van der Waals contacts and hydrogen bonds with the phosphate groups and the ribose of the cap analog further stabilize the cap-eIF4E interaction (Niedzwiecka et al., 2002). Nucleotides downstream of the cap also influence eIF4E binding, but no intermolecular contacts beyond the first nucleotide after the cap structure have been detected. The equilibrium binding constant of eIF4E to cap analog varies from 0.1 to 4 μM depending on the experimental conditions and source of protein (Carberry et al., 1991; Niedzwiecka et al., 2002). eIF4G binds eIF4E on the convex side, away from the cap-binding pocket, causing structural changes (Gross et al., 2003) that increase the cap-binding affinity of eIF4E (Haghighat and Sonenberg, 1997; von der Haar et al., 2004).

On cell entry, the RNA of an invading positive strand RNA virus must compete aggressively for the limiting translational machinery. Because these viruses replicate in the cytoplasm without access to the nuclear capping machinery, many viral RNAs lack a 5′ cap. Instead, they rely on sequences that functionally replace, and are often more efficient than, the 5′ cap structure for translation initiation. These sequences include internal ribosome entry sites (IRESes) and 3′ cap-independent translation elements (3′ CITEs). IRESes are located upstream of the translated open reading frame (ORF) and recruit the ribosome via a variety of mechanisms (Doudna and Sarnow, 2007). To date, 3′ CITEs are known to exist only in plant viral RNA 3′ UTRs and possibly the 3′ UTR of p53 mRNA (Chen and Kastan, 2010). Among the several classes of these elements (Miller et al., 2007), the Satellite tobacco necrosis virus (STNV) translation enhancer domain (TED), and an "I-shaped" CITE from Maize necrotic streak virus (MNeSV) have been shown to bind eIF4F (Gazo et al., 2004; Nicholson et al., 2010). The Barley yellow dwarf virus (BYDV)-like translation element (BTE) binds the eIF4G subunit of eIF4F and does not require eIF4E (Treder et al., 2008). Recently, we showed that a new class of element (PTE), first identified in Panicum mosaic virus (PMV) (Batten et al., 2006), and then in Pea enation mosaic virus RNA 2 (PEMV2), binds and requires eIF4E (Wang et al., 2009). Most 3′ CITEs are predicted or known to base pair to the 5′ UTR (Guo et al., 2001; Fabian and White, 2004; Rakotondrafara et al., 2006; Nicholson et al., 2010). Presumably this circularizes the mRNA, allowing the 3′ CITE-bound initiation factors to recruit the ribosome 40S subunit to the 5′ end, from which it moves to the first AUG.

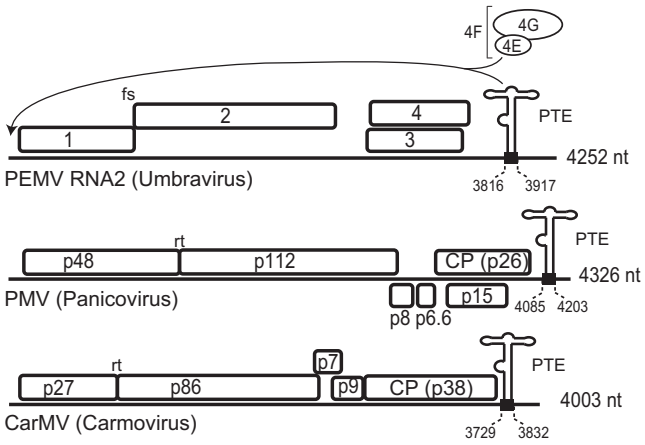

Figure 1. Genome Organizations of Representative Viruses in the Umbravirus, Panicovirus, and Carmovirus Genera that Contain a PTE in the 3′ UTR

Genome lengths are shown at right. Numbered boxes indicate open reading frames. PTEs in PEMV RNA2 (Wang et al., 2009) and PMV (Batten et al., 2006) have been described. CarMV PTE is described in this article. Long, curved arrow indicates binding of eIF4F (via the eIF4E subunit) to the PTE, and interaction of this complex with the 5′ end. This proposed mechanism applies to all viruses with 3′ PTEs. Ribosomal frameshift (fs) or read-through (rt) events facilitate translation of the second ORF. ORFs further downstream are translated via initiation at multiple start codons on subgenomic mRNAs.

Here we investigate how the PTE RNA binds eIF4E, despite lacking a 5′ cap. We use phylogenetic comparisons of several newly described PTEs, structural probing and computer modeling to predict that the PTE forms a compact pseudoknot that projects a guanosine residue into the cap-binding pocket of eIF4E. This would be a new way of mRNA recognition by a translation initiation factor.

RESULTS

Three Virus Genera Contain Similar 3′ PTE-Like Structures

The PTE, identified previously in the 3′ UTR of PEMV2 (Figure 1), consists of a long bulged helix bifurcating into two stem loops. A large G-rich bulge (G domain) exists in the middle of the main helix (Figure 2). Previous structure probing of the PEMV2 PTE suggested that a C-rich bulge (C domain), on the branch point of the distal helices, base pairs to a three guanosine tract in the G domain to form a pseudoknot (Wang et al., 2009). The PTEs of PMV and PEMV2 are predicted to fold into very similar structures, despite absence of sequence homology outside of the G and C domains (Batten et al., 2006; Wang et al., 2009).

To determine whether the PMV PTE folds like the PEMV2 PTE as predicted, and to obtain more evidence on interaction of the C and G domains, we probed both PTEs using SHAPE (Wilkinson et al., 2005) as described previously (Wang et al., 2009), except the more rapid acylating agent 1M7 (Mortimer and Weeks, 2007) was used instead of NMIA. The RNAs were probed in the presence and absence of magnesium ion. Magnesium ion favors tertiary interactions such as pseudoknots. We also compared wild-type PTEs with mutants containing transversions in the C domain designed to disrupt the G domain-C domain base pairing. These mutations are known (PEMV2m2) or predicted (PMVm1) to prevent the cap-independent translation function of the PTE. The gel profiles and corresponding structures of wild-type PEMV2 and mutant PEMV2m2 PTEs probed with 1M7 were similar to those found previously with NMIA (Wang et al., 2009). In the presence of Mg^{2+}, one guanosine (G_{3840} in PEMV2 and G_{4133} in PMV) in the G domain was hypermodified by 1M7, whereas the flanking G domain nts were modified moderately, and none of the Cs in the C domain was modified. In contrast, in C-domain mutants PEMV2m2 and PMVm1, the entire G domain became significantly and more evenly modified and the C domain was modified to a greater extent than in wild-type PTEs (Figure 2). These results are consistent with these domains being single stranded in the mutant RNAs, as expected. Strikingly, the modification patterns of both wild-type PTEs in the absence of Mg^{2+} were very similar to the modification patterns of the mutant PTEs in the presence of Mg^{2+} (Figure 2A). In both cases the pseudoknot is not predicted to form. We conclude that, in wild-type PTEs, pseudoknot base pairing between the C and G domains takes place in a Mg^{2+}-dependent manner, and that the PEMV2 and PMV PTEs fold into very similar tertiary structures as predicted. However, the magnesium-dependent hypermodified G in the pseudoknot is not predicted to be so accessible to acylation, thus it may be in a novel orientation (see below).

To better understand the sequence and structural requirements of the PTE, more phylogenetic comparisons were undertaken by predicting secondary structures in the 3′ UTRs of related viruses, using MFOLD (Zuker, 2003). Two recently sequenced panicoviruses, the phleum isolate of Cocksfoot mild mosaic virus (CMMV) (Ziegler et al., 2009) and Thin paspalum asymptomatic virus (TPAV) have PTE-like predicted structures in their 3′ UTRs. Moreover, the 3′ UTRs of five carmoviruses, which, like the panicoviruses, are in the Tombusviridae family, harbor predicted PTE-like structures.

The secondary structures of all of these putative PTEs were determined using SHAPE (Figure 3). They share the following features (Figure 4; see Table S1 available online): (1) a basal helix connects the element to the rest of the viral genome, interrupted by small proximal bulges of no more than two unpaired bases; (2) the large G domain bulge ranging from 6 (CarMV) to 14 (HCRSV) nt, always contains a G that is hypermodified by SHAPE reagents in a magnesium dependent structure (Figure 3, arrow); all G domain bulges, except that of JINRV, contain a GGG tract, which is complementary to the C domain; (3) helix 3 (H3) consists of 6–8 bp, although in some PTEs (e.g., HCRSV and PFBV) some of these bases are SHAPE modified and thus unlikely to be stably base paired; (4) branching stem-loops (SL1 and SL2), each usually contain 4–7 bp, but range from 3 to 12 bp; (5) loop 1 has a UGC[A/C] motif in all but three of the PTEs. Loop 1 of the panicovirus PTEs has six bases complementary to the 5′ UTR, whereas in the other PTEs, the complementary tract is shorter (Figure 4, italics); this conserved complementarity suggests a role for long-distance base pairing to the 5′ UTR; (6) the C-domain bulge between SL1 and SL2 is 4–6 (usually 4) nt long; the C domain has a CCC tract that appears to base pair to the GGG tract in the G domain except in SCV in which CUU in the C domain can base pair to the GGG, and JINRV in which

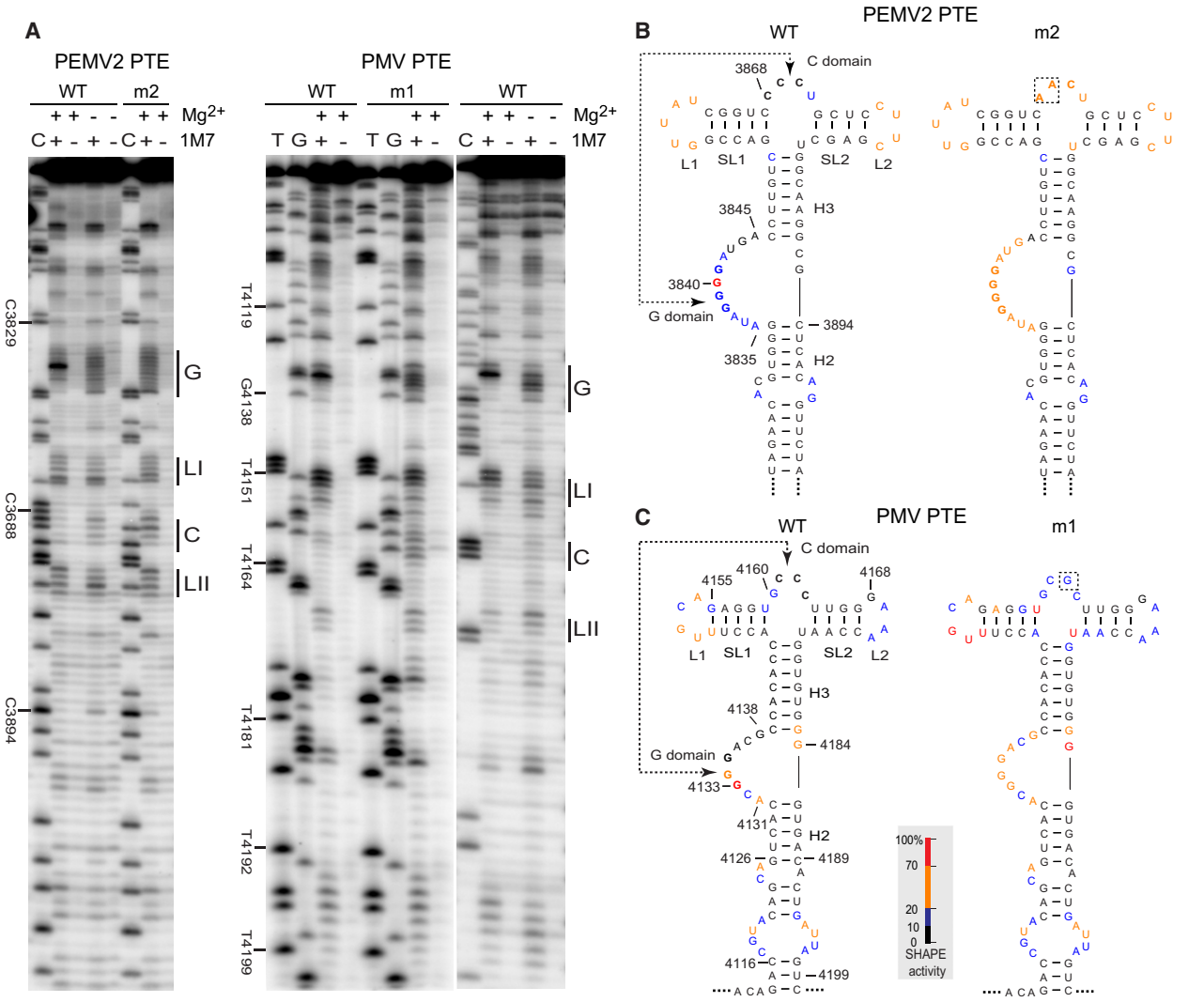

Figure 2. Effects of Magnesium and Mutations in the C Domain on PTE Structure

(A) Structure probing by SHAPE of PTEs of PEMV2 and PMV. Presence of SHAPE reagent 1M7, and Mg^{2+} is indicated by + above each lane. Sequencing ladders generated by reverse transcription in the presence of dideoxy NTPs are in lanes marked C, T or G. Mobilities of selected nucleotides are indicated to the left of each gel. Positions of G domain (G), loop I (LI), C domain (C), and loop II (LII) are indicated to the right of each gel. Probed RNAs include wild-type (WT) or mutant m2 of PEMV2 PTE, or WT or mutant m1 of PMV PTE.

(B) Secondary structures of PTEs probed in (A). Dashed boxes highlight the altered nucleotide(s). Double-headed-arrows indicate the pseudoknot interaction between G and C domains. Color-coded bases indicate the level of 1M7 modification with warmer colors indicating greater modification (inset).

the CCC tract has no obvious Watson-Crick base pairing partners in the G domain; and (7) the number of unpaired bases connecting H3 and H2, opposite the G domain, ranges from zero to one nt in most cases, but is two nts in PEMV2, and 7 nts long in HCRSV.

The PTE-Like Structures of Panicoviruses and Carmoviruses Are Functional CITEs

Free 3′ CITEs, from all viruses tested, can inhibit translation in *trans* as isolated RNAs not attached to an mRNA. This *trans*-inhibition correlates with efficiency of stimulation of translation by the 3′ CITE in *cis* (as part of an mRNA) (Treder et al., 2008; Wang et al., 2009, 2010; Nicholson et al., 2010). To determine whether the putative PTEs were functional, we tested the abilities of the RNAs to *trans*-inhibit translation of an mRNA in wheat germ extract. All nine PTEs inhibited translation to between 15% and 40% of the level obtained in the absence of *trans*-inhibitor (Figure 5). The levels of inhibition are similar to those obtained with the unrelated BTE of BYDV (25%) and the STNV TED (30%). Interestingly, the strongest *trans* inhibitor, the HCRSV PTE, (Figure 5), deviates most from consensus with longer bulge sequences and longer pseudoknot base pairing (AGGGG:CCCCU) (Figure 4). As a negative control, the nonfunctional mutant, PEMV2m2, inhibited translation only slightly in *trans* (PEMV2m2, Figure 5). Thus, all of the proposed PTEs are functional, inhibiting translation in *trans* probably by binding and sequestering eIF4E.

Despite the similarities in structure of the PEMV2 and PMV PTEs, neither the C-domain nor the G-domain, nor both

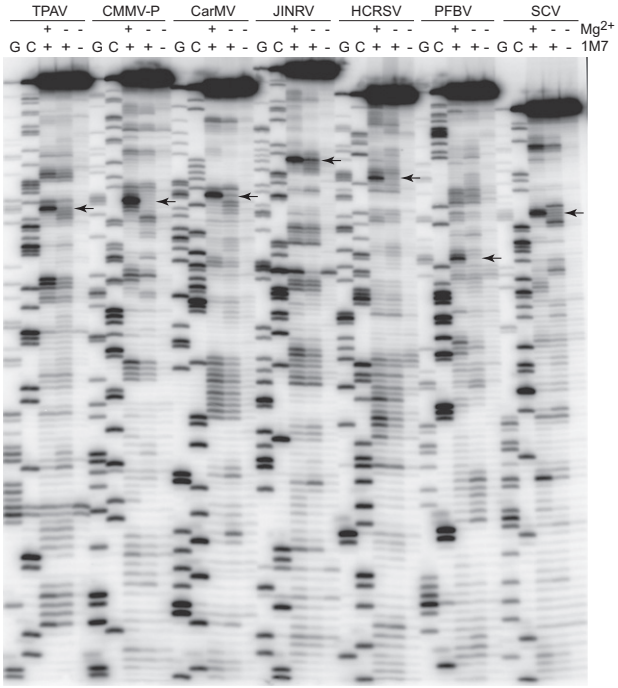

Figure 3. SHAPE Probing of Putative PTEs of Panicoviruses and Carmoviruses in the Presence or Absence of Mg^{2+}

Plus signs (+) indicate presence of Mg^{2+} or 1M7. G and C sequencing ladders are indicated above each lane. Arrows show the Mg^{2+}-dependent hyper-modified guanosine.

in combination with the unpaired bases opposite the G domain, could be exchanged between these PTEs and yield a functional PTE (Figure S1). Thus, the G and C domains depend on very specific contexts to fold into active structures.

3D Modeling of the PTE

To understand how the PTE functions and interacts with eIF4E, we computationally predicted its 3D structure. To guide the modeling, we first assumed that all PTEs fold into the same 3D shape, as their secondary structures are similar and they perform the same function. The second assumption is from observations that RNA structures often present a view in which all base edges are visible (Laederach et al., 2007). Third, we assumed that helices tend to coaxially stack, allowing an uninterrupted helix in at least one strand, optimizing base stacking and shielding their hydrophobic rings from water (Levitt, 1969).

To determine the consensus 3D model we first aligned sequences based on secondary structure (Figure 6A). The sequence of HCRSV PTE was omitted from the modeling, owing to the large bulge sequences and long SL2, which skewed the data used for determining the consensus 3D fold. The tertiary structure for PMV was sketched first using the Nucleic Acid Simulation Toolkit (NAST) (Jonikas et al., 2009). NAST represents the RNA as a chain of beads (one per nucleotide) evolving under forces originating from a potential energy function derived from solved RNA structures. This allowed us to rapidly test whether the pseudoknot could be accommodated in the 3D fold, and provided us with valuable information about the potential global shape of the molecule, especially on the coaxial stacking of the helices.

Using the computer program MC-Sym (Major, 2003; Major et al., 1991) combined with nucleotide cyclic motifs (NCM) (Parisien and Major, 2008), we generated 10,000 3D models for each PTE sequence in Figure 6A. Using the P-Score, we identified the top hundred folds for each sequence (see Experimental Procedures). The P-Score encodes long-range RNA 3D information, in contrast to classical mechanical force fields that better describe local interactions. Local interactions in MC-Sym models, and in particular those in NCMs conform to current knowledge on atomic interactions because they stem from fragments of solved structures. The consensus 3D structure was then determined by choosing the folds with the least pairwise root-mean-square deviation (rmsd) with one another (Figure 6B). Pairwise rmsd ranges from 2.09 to 4.05 (Table S2). An all-atoms model for the PMV PTE (Figure 6C) incorporated the predicted pseudoknot and coaxial stacking, as it features A-RNA-like helices and a smooth backbone path throughout. The few unpaired nucleotides in the pseudoknot region caused a fixed juxtaposition of the two main axes at nearly a 90° angle.

The 3D model readily explains the requirement for magnesium ion to counter the electrostatic repulsion of multiply converging strands around the pseudoknot (Figures 2 and 3). It also explains the poor SHAPE-reactivity of the C-domain and the uracil linking SL2 to H3 (Figure 4), because they are buried in the core of the pseudoknot. Although the SHAPE-hypermodified guanosine residue (Figures 6B and 6C, red) is predicted to be base paired, it is on the surface at a sharp bend in the RNA backbone that may permit it to protrude in from the helix as suggested by the extreme acylation by 1M7 and NIMA.

eIF4E Binds the PTE via the G Domain

Previous analysis of the PEMV2 PTE mutants showed strong correlation between eIF4E binding affinity and translation stimulation activity (Wang et al., 2009). Therefore, we sought to determine the structural basis for binding of the uncapped PTE RNA by eIF4E. To localize the protein binding site in the RNA, we applied a footprinting assay by probing the PTE with 1M7, and RNases T1 and V1 in the presence of increasing quantities of eIF4E. In both PTEs, the presence of eIF4E had little effect on cleavage or modification of most nucleotides, indicating that eIF4E binding does not cause major conformational change in the PTE. For example, nucleotides in loops 1 and 2 were modified or cleaved the same in the presence or absence of eIF4E (Figure 7; Table S3). In the absence or presence of eIF4E, almost no RNase T1 cleavage of the only G (G4160) in the C domain of PMV was detected, supporting the notion that the C domain is constrained, and that G4160 pairs in a non-Watson-Crick interaction to A4136 in the pseudoknot (Figure 6C). Also in the absence of eIF4E, the three consecutive Gs in the middle of the PMV G domain generated <20% RNase T1 cleavage compared to G4152 of loop 1 (L1), supporting participation by the three Gs in pseudoknot base pairing to the C domain. Similar observations were made of the PEMV2 PTE, but G3858 in loop I was not cleaved by RNase T1, suggesting that it base pairs to the U3862 on the opposite side of the loop.

In both PTEs, the G tract in the G domain became less accessible to RNase T1 cutting and to 1M7 modification as the

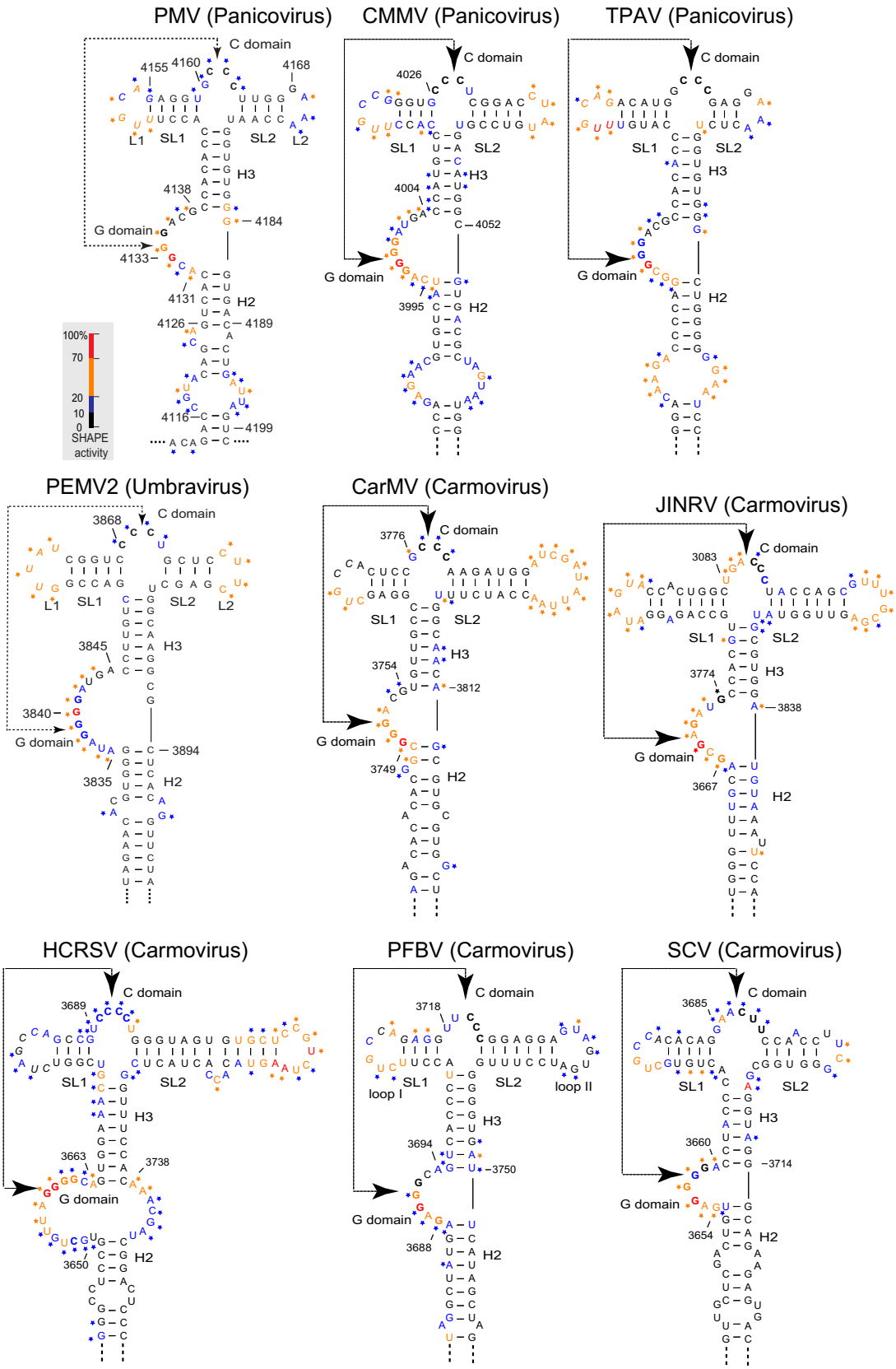
PMV (Panicovirus)
CMMV (Panicovirus)
TPAV (Panicovirus)
PEMV2 (Umbravirus)
CarMV (Carmovirus)
JINRV (Carmovirus)
HCRSV (Carmovirus)
PFBV (Carmovirus)
SCV (Carmovirus)
C domain
G domain
SL1
SL2
L1
L2
H2
H3
loop I
loop II
100%
70
20
10
0
SHAPE activity

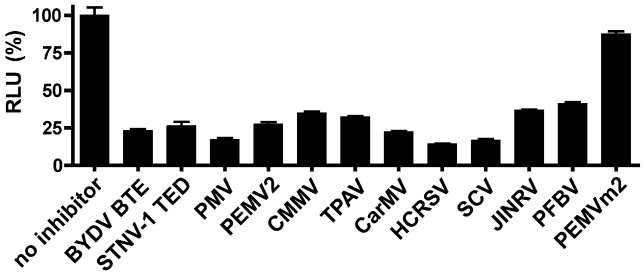

Figure 5. *trans*-Inhibition Assay of Putative PTEs and Other CITEs
The indicated RNAs were added in a 100-fold molar ratio to a very efficiently translated mRNA consisting of the BYDV 5′ and 3′ UTR flanking a firefly luciferase ORF. After incubation in a wheat germ translation extract, relative light units (RLU) were measured in a luciferase assay (Experimental Procedures). Luciferase expression is presented as a percent of that obtained in the absence of added CITE. The BYDV BTE and STNV-1 TED are CITEs unrelated in sequence or structure to the PTEs. PEMV2m2 contains the C domain mutations (Figure 2B) that prevent PTE function in *cis* (Wang et al., 2000). Samples were assayed in triplicate and error bars indicate standard error. See also Figure S1.

concentration of eIF4E increased (Figure 7). Some cleavages by RNase V1, which cleaves certain double-stranded or stacked nucleotides in a nonsequence specific manner (Lowman and Draper, 1986), increased or decreased in the presence of eIF4E. In both PEMV2 and PMV PTEs, RNase V1 cut strongly around the junction region between SL1 and H3 in the presence of eIF4E. This indicates that eIF4E binding facilitates coaxial stacking of H3 and SL1 as predicted in the 3D model, and does not protect this region from access to nuclease V1 (Figure 7). The decreases in 1M7 modification or changes in cleavage due to eIF4E are localized mostly around the pseudoknot and H2 and H3, suggesting that this region is the eIF4E binding site. More distant changes in V1 sensitivity may be due to alterations in RNA structure rather than direct blockage by eIF4E.

Docking of eIF4E on the PTE In Silico

Finally, we predict the 3D interaction of eIF4E with the PTE using the above protection data and the known structure of eIF4E. In binding eIF4E, the m^7G cap is sandwiched between two tryptophan residues (W62 and W108) of the cap-binding pocket (Marcotrigiano et al., 1997; Monzingo et al., 2007). Mutation of these amino acids to leucine caused eIF4E not to bind the PTE; thus the cap-binding pocket of eIF4E is essential for binding to the PTE (Wang et al., 2009). We hypothesize that, in the presence of eIF4E, the hypermodifiable G of the PTE is bound in the cap-binding pocket by similar interactions. To test this possibility, using MC-Sym, this G was placed in the pocket in the same coordinates as m^7G. With this constraint, the best possible structures generated by MC-Sym that had no steric clashes were selected. We found structures that show good fit between eIF4E and the pseudoknot region of the PTE (Figure 8). The orientations of the PMV and PEMV2 PTEs relative to eIF4E differ, but in both cases the hypermodifiable G stacks between the tryptophan residues in the cap-binding pocket, whereas loops that form the rim of the pocket clamp around the pseudoknot. This interaction would be expected to leave most of the PTE unprotected in the footprinting assays. Indeed, the binding site agrees with the RNase T1 and SHAPE protection data, in that eIF4E is predicted to interact most closely with the pseudoknot region (the G domain strand in particular) and the adjacent part of H2. Moreover, the portion of H3-SL1 junction that shows increased V1 sensitivity in the presence of eIF4E is not predicted to be protected by eIF4E. It is possible that binding by eIF4E induces small structural changes in the PTE that enhance H3-SL1 helical stacking distant from the eIF4E binding site. Overall, these data provide a compelling new model by which an uncapped RNA may bind the cap-binding factor eIF4E.

DISCUSSION

The PTE Structure Is Conserved in Three Virus Genera

We report structures that resemble PTEs in all three known panicoviruses, one umbravirus, and five carmoviruses. (The first carmovirus PTE was discovered in SCV and communicated to us by Anne Simon, University of Maryland.) Structure probing (Figures 2 and 3) and the phylogenetic comparisons among the PTE structures (Figure 4) revealed common features of the PTEs that could be modeled to produce a remarkably consistent 3D structure (Figure 6). Based on their ability to inhibit translation in *trans* (Figure 5), it is highly likely that all of these PTEs are functional translation enhancers in *cis*.

A requirement for long-distance base pairing to the 5′ UTR has been demonstrated for the 3′ CITEs of BYDV (Guo et al., 2001; Rakotondrafara et al., 2006), TBSV (Fabian and White, 2004), and MNeSV (Nicholson et al., 2010), which are unrelated to the PTE or each other, supporting the model that the 3′ CITE binds one or both subunits of eIF4F and delivers it to the 5′ UTR by long-distance base pairing (Treder et al., 2008; Nicholson et al., 2010). Loop 1 of the three panicovirus PTEs has 6 complementary bases to the 5′ UTR (Figure 4, italics). In the other viruses, which have fewer 5′-complementary bases in loop 1, 3′ UTR sequences adjacent to the PTE may base pair to the 5′ UTR. Indeed, base pairing of a sequence immediately upstream of the SCV 3′ PTE is required for efficient translation (A. Simon, personal communication).

A portion of the 3′ UTR that contains the HCRSV PTE was reported previously to be required for cap-independent translation, although the PTE was not identified (Koh et al., 2002). Mutations in the sequence $_{3659}$GGGCAG$_{3664}$ reduced translation of uncapped RNA five-fold (Koh et al., 2003). These bases include the SHAPE-hypermodified G_{3659} and three G domain bases expected to base pair to the C domain (Figure 4). These observations support the requirement for the pseudoknot, which the mutations disrupt.

Figure 4. Secondary Structures of PTEs
Results of solution structure probing from Figure 2 and Figure 3 are superimposed on the best fitting secondary structures. Color-coded bases indicate the level of 1M7 modification (Table S1) with warmer colors indicating greater modification (inset). Colored asterisks indicate modification level in absence of magnesium. Bases in bold participate in predicted pseudoknot base pairing. Bases in italics (in SL1) are predicted to base pair to the 5′ UTR.

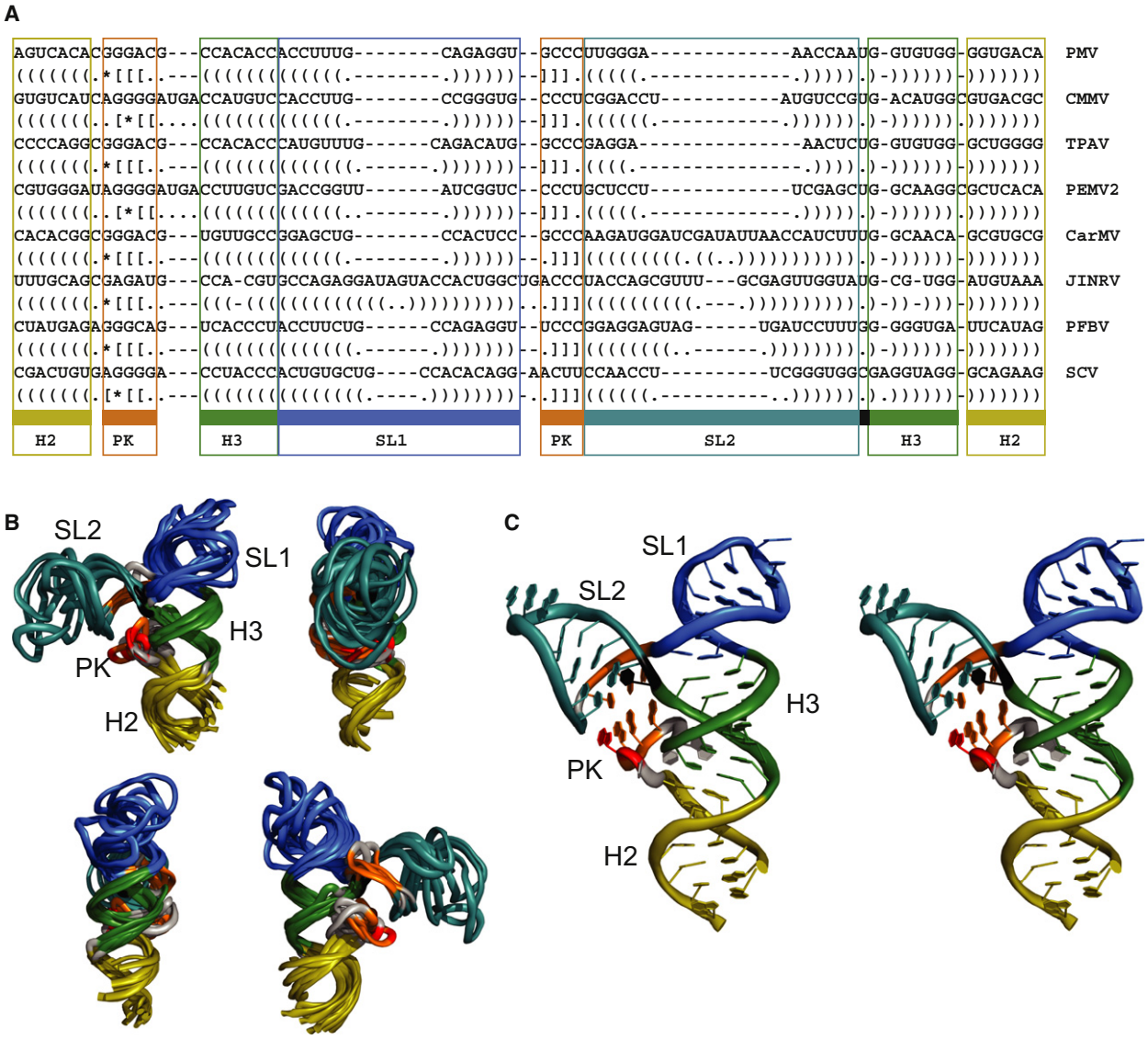

Figure 6. Consensus Structure of the PTE Elements

(A) Color-coded sequence alignment based on the secondary structures. Corresponding base pairs are highlighted using left and right parenthesis whereas pseudoknotted (PK) base pairs are shown with left and right square brackets. Unpaired nucleotides use ".". Gaps in the alignment use "–". The base (usually a U) between SL2 and H3 is indicated by a black bar

(B) Optimal superposition of the 3D models for the PTE elements (pairwise rmsd is in Table S2). Only the backbone trace is shown for clarity. The models align base paired positions that are common in all secondary structures. Colors are the same as in (A), except the highly reactive guanosine is in red.

(C) Stereo view of the PMV PTE element. Here, the bases are rendered as slabs. Colors are the same as in (B). PDB files of all predicted PTE structures are downloadable at http://www.plantpath.iastate.edu/millerlab/node/30.

The only 3′ CITE for which a 3D structure has been determined is the ribosome binding structural element (RBSE) of Turnip crinkle virus (TCV), a carmovirus. It differs in secondary structure from the PTE, and its 3D structure roughly resembles a tRNA (Zuo et al., 2010). The RBSE binds yeast 60S ribosomal subunits (Stupina et al., 2008) but its initiation factor binding properties are unknown. The presence of different classes of 3′ CITE (RBSE or PTE) in different carmoviruses reiterates our previous observations that the class of element in any particular virus does not necessarily correlate with viral genome phylogeny (Miller et al., 2007; Wang et al., 2009).

A Structural Explanation for eIF4E Binding to the PTE

To model how the PTE can bind with such high affinity while lacking the 7-methyl group and the triphosphate that are crucial for cap binding to eIF4E, we first consider the RNA structure. The PTE pseudoknot appears to differ from others (Taufer et al., 2009) because it is embedded in the 3D structure such that it forces a stretch of guanosines (the G-rich region) into an unusual fold. The juxtaposition of sequence and structure at the apex of the pseudoknot may provide a unique context that attracts eIF4E with high affinity. Furthermore, the G- and C-rich domains cannot be exchanged between PTEs without loss of function,

nor can the G domain and the unpaired bases on the opposite side of the H2-H3 helix be simultaneously exchanged with those from other PTEs (Figure S1). This argues for a special condition for high-affinity eIF4E binding. Even though eIF4E usually binds to the cap of a single-stranded RNA, its extensive electropositive field around the cap-binding pocket (Figure S2) should permit it to bind a structured RNA. Comparison of the 3D structures between the m^7G-bound form and the predicted PTE-bound form shows that the protein structure is essentially the same (0.1 Å rmsd).

The PTE structure may not be equally stable or rigid in all regions. In particular the pseudoknot seems to "breathe." The G domain is partially susceptible to SHAPE modification with the striking exception of the 1M7-hypermodifiable G, and is partially cleaved by T1 nuclease. The absence of magnesium or mutation of the C domain cause a virtually identical loss of extreme SHAPE modification, and more uniform modification of the entire G domain bulge, as if single-stranded, strongly supporting the existence of the pseudoknot in the native, functional PTE (Figure 2; Table S1). SHAPE reagents such as 1M7 are thought to modify only single-stranded nucleotides, because they are flexible and transiently form conformations in which the 2′ hydroxyl is far enough from the adjacent 3′ phosphodiester oxygens to allow access by the acylating agent (Wilkinson et al., 2005). In contrast, the 2′ hydroxyl in Watson-Crick base paired nucleotides in the A-form double helix is too close to the adjacent 3′ phosphate, sterically hindering access by the SHAPE reagents (Merino et al., 2005). We propose that the hypermodifiable G is not part of a typical A-form double helix, but held in an orientation by the pseudoknot and flanking bases that render its 2′ hydroxyl constantly and highly accessible to 1M7 and NIMA. Thus, the G may protrude from the PTE structure, and be capable of fitting in the cap-binding pocket of eIF4E (Figure 8). There is precedent for such an orientation of a nucleotide from a pseudoknot. The well-characterized, but much simpler pseudoknots that facilitate frameshifting in polerovirus and enamovirus RNAs feature a base at the helical junction region that protrudes into solvent, held in place by non-Watson-Crick interactions of flanking bases (Giedroc and Cornish, 2008; Su et al., 1999). To our knowledge, such pseudoknots have not been SHAPE probed so it isn't known if the protruding nucleotide is highly acylatable. An alternative possibility is that the hypermodifiable G is base paired in the pseudoknot, but the kink in the backbone makes its 2′ hydroxyl accessible. Interactions of the rim of the cap-binding pocket with the pseudoknot may induce a conformational change in which the guanosine inserts into the pocket.

The footprinting data (Figure 7) and previous mutagenesis of the eIF4E cap-binding pocket (Wang et al., 2009) are consistent with the cap-binding pocket-pseudoknot interaction model (Figure 8). Because the PTE lacks the 7-methyl group and triphosphate necessary for m^7GTP binding, yet the affinity of eIF4E for the PTE (58 nM) is apparently stronger than that of eIF4E for m^7GTP (Niedzwiecka et al., 2002; Wang et al., 2009), we speculate that additional contacts between the surface amino acids around the cap-binding pocket, which may clamp around the pseudoknot (Figure 8), enhance binding affinity to the PTE. Indeed the vast majority of mutations in the PEMV2 PTE near (in the predicted 3D structure) the hypermodifiable G are highly deleterious to PTE function (Wang et al., 2009).

The PTE-eIF4E Interaction Differs from IRESes and Other CITEs

Plant virus 3′ CITEs fall into about seven structural classes (Miller et al., 2007). The Y-shaped (Fabian and White, 2004), I-shaped (Nicholson et al., 2010) CITEs and BTEs (Rakotondrafara et al., 2006) all require ribosome scanning from the 5′ end, and do not function as IRESes. The only IRES known to require eIF4E is that of Hepatitis A virus (HAV) (Ali et al., 2001). Whether the HAV IRES interacts directly with eIF4E is unknown. Recently, an eIF4E-binding motif, consisting of two short adjacent stem-loops, was described in the coding region of mouse histone H4 mRNA (Martin et al., 2011). It is required for a novel cap-dependent, UTR-independent translation mechanism, and it binds the N-terminus of eIF4E, not the cap-binding pocket. A similar shaped eIF4E binding structure, but required for nuclear export and not translation, is located in the 3′ UTR of cyclin D mRNA (Culjkovic et al., 2006). Thus, eIF4E-binding by uncapped mRNAs has evolved for numerous functions.

Viruses with PTEs have short 5′ UTRs with complementarity to the PTE (or nearby bases), so the ribosome probably enters at the 5′ end as with other 3′ CITEs. However, the HCRSV 3′ UTR, which includes a PTE, also has been reported to facilitate internal initiation in combination with an IRES located in the middle of the viral genome (Koh et al., 2003). Interestingly, the I-shaped CITE in the 3′ UTR of Melon necrotic spot virus (MNSV) appears to interact with eIF4E, based on genetic evidence (Truniger et al., 2008). A single point mutation (H228L) on the rim of the cap-binding pocket greatly reduces the ability of most strains of MNSV to translate efficiently; thus this eIF4E allele is a recessive resistance gene (Nieto et al., 2006). Mutations in the I-shaped structure permit MNSV translation in the presence of the mutant eIF4E, and allow the virus to break the resistance (Truniger et al., 2008). Thus, like the PTE, the I-shaped domain requires eIF4E. A similar I-shaped 3′ CITE in MNeSV binds efficiently only to eIF4F and not eIF4E or eIF4G alone (Nicholson et al., 2010). Thus, the I-shaped domain may bind eIF4E only when eIF4E is bound to eIF4G. Like the I-shaped structure, the STNV TED binds eIF4F with far higher affinity than to eIF4E or eIF4G (Gazo et al., 2004), whereas the BTE binds and requires only eIF4G, although translation is stimulated slightly more by eIF4F (Treder et al., 2008). In summary, none of these characterized CITEs resembles the PTE in structure or in their interactions with translation factors.

We propose that the various CITEs have evolved to bind different surfaces on eIF4F, and then deliver it to the 5′ end by long-distance base pairing (Figure 1) (Miller et al., 2007). In support of this mechanism, the interaction of the cap-binding pocket of eIF4E with the PTE pseudoknot leaves both the eIF4G-binding convex surface of eIF4E and loop 1 of the PTE unaffected and solvent accessible (Figure 8). This should allow eIF4E to bind simultaneously to eIF4G (forming eIF4F) and to the PTE. Indeed it has a higher affinity for eIF4F than eIF4E (Wang et al.,. 2009). This eIF4F-bound PTE can then base pair to the 5′ UTR via loop 1, circularizing the RNA and placing eIF4F in close proximity to the 5′ end where it can then recruit the ribosome.

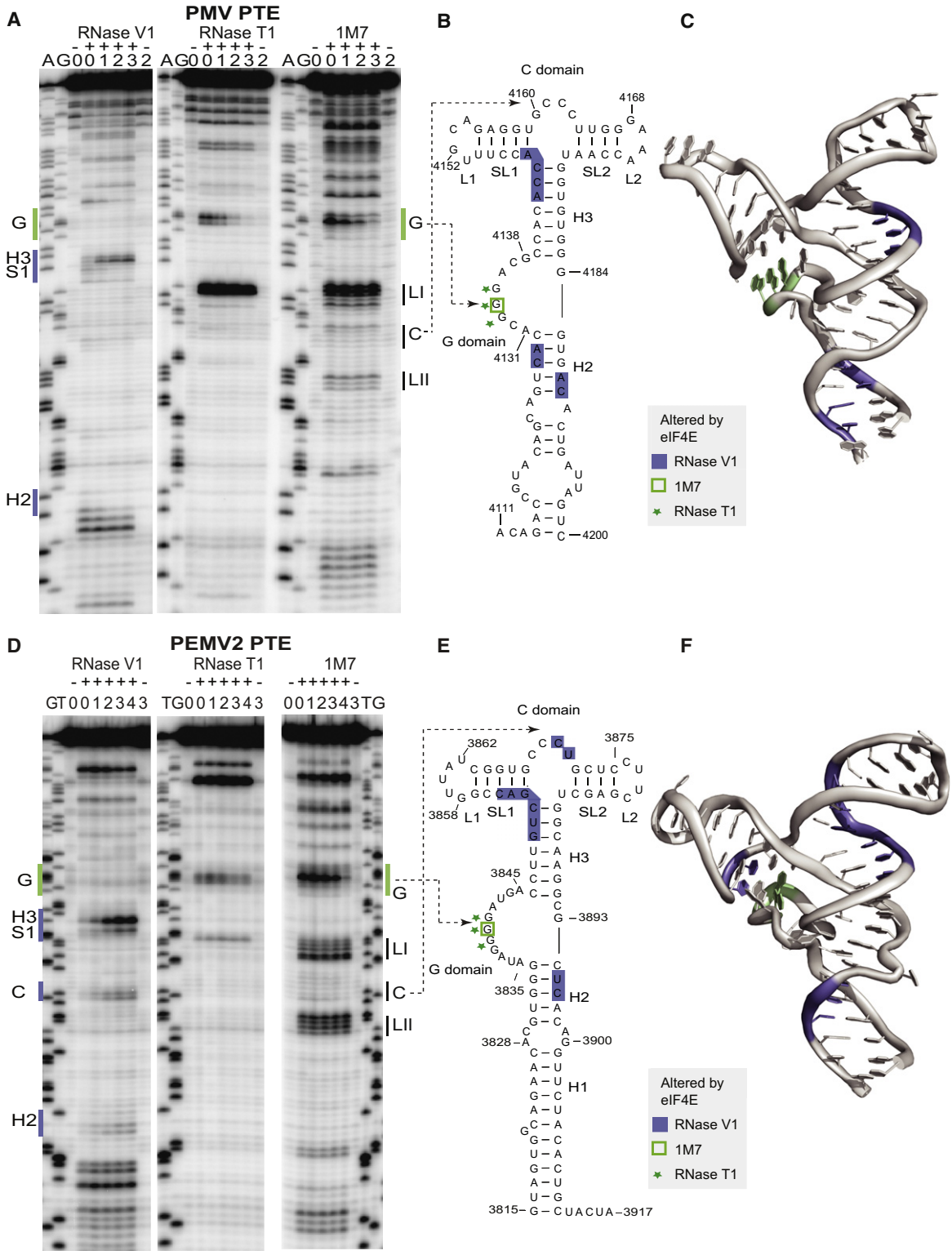

Figure 7. Footprinting by Treatment of PTEs with RNase V1, RNase T1, or 1M7 in the Presence of Increasing Concentrations of eIF4E

(A) Concentration of eIF4E added to PMV PTE (μM): 0 (lanes 0), 0.1 (lanes 1), 0.5 (lanes 2), 2.0 (lanes 3).

(B) Secondary structure of PMV PTE indicating bases that show reduced modification by 1M7 (green asterisks), or reduced cleavage by RNase T1 (green shading) or altered cleavage by RNase V1 (blue shading) in the presence of increasing quantities of eIF4E. See also Table S3.

(C) Predicted 3D structure of PMV PTE with the regions showing reduced modification or cleavage due to eIF4E are color coded as in (B). Green indicates regions showing reduced modification by either 1M7 or RNase T1.

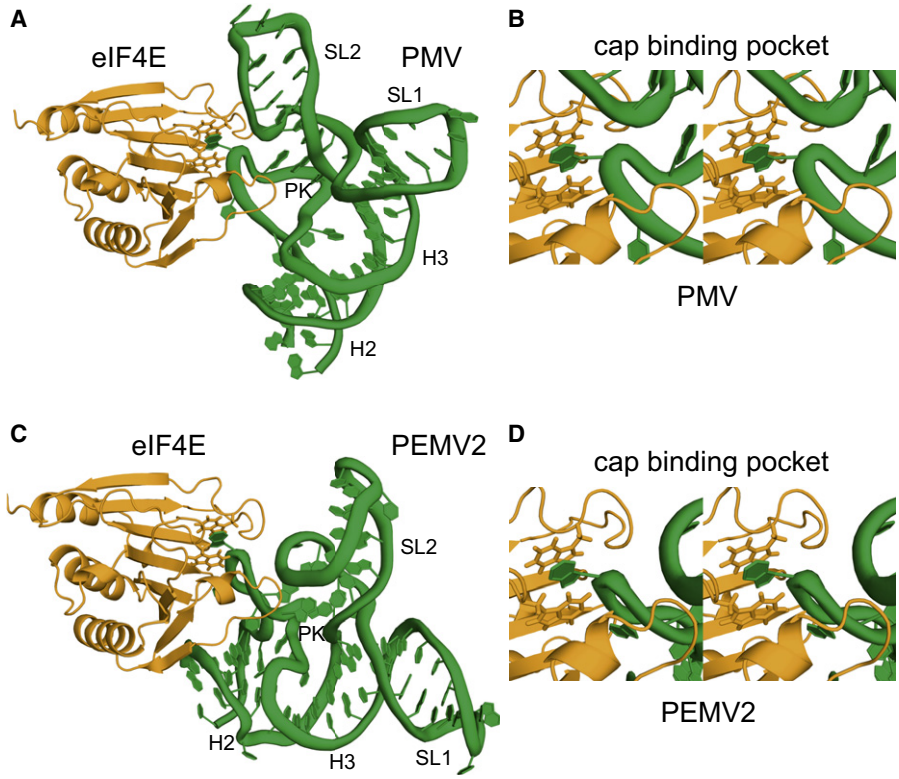

Figure 8. Model of eIF4E Docking on the PTE

(A) The wheat eIF4E protein (PDB file 2IDV) (yellow), docked on the PTE (green) was modeled by placing the hypermodifiable guanosine of the PTE, in place of the known coordinates of m7G, between two eIF4E tryptophan side-chains (rendered as sticks).

(B) A close-up stereo view of the docking site.

(C) Wheat eIF4E (yellow) docked on the PEMV2 PTE (green) as in (A).

(D) Close-up of docking site in (C). Files specifying the atomic coordinates of these structures are downloadable at http://www.plantpath.iastate.edu/millerlab/node/30.

EXPERIMENTAL PROCEDURES

Plasmid Constructs and RNA Preparation by In Vitro Transcription

DNA oligomers representing PTEs from the following viruses were synthesized and inserted between EcoR I and HpaI sites of the universal SHAPE vector as described (Wang et al., 2010) (GenBank number, sequence in parentheses): PMV (NC_002598, nt 4085–4201) (Batten et al., 2006), CMMV (EU081018, nt 3959–4092), CarMV (X02986, nt 3716–3845), JINRV (D86123, nt 3738–3870), HCRSV (NC_003608, nt 3634–3761), PFBV (NC_005286, nt 3641–3770), SCV (U72332, nt 3627–3748), and TPAV (PVBE database, ftp://ftp.genome.ou.edu/pub/PVBE/PVBE_all.fa, contig tgp_p06_05TGP00369_GTGT_contig00009, nt 3001–3133). The resulting constructs were linearized with SmaI as the templates for RNA transcription in vitro using MEGAshortscript (Ambion). PEMV2 PTE was generated as described previously (Wang et al., 2009).

RNA Activity Assay by *trans* Inhibition Assay In Vitro

For RNA competition experiments in wheat germ extract, 0.4 pmol of reporter RNA P2lucP2 (Wang et al., 2009) was mixed with 40 pmol of competitor RNA in a 50 μl translation assay mixture. After 1 hr at room temperature, luciferase activity was measured using the luciferase assay reporter system (Promega) in a GloMax20/20 Luminometer (Promega).

Recombinant Protein Expression and Purification

Recombinant wheat eIF4E was expressed from pGEXw4E vector as described previously (Wang et al., 2009). Briefly, GST-tagged eIF4E was induced with 0.2 mM IPTG at 30°C for 6 hr. GST-eIF4E was immobilized on the glutathione-SepharoseTM 4B (Amersham Biosciences) column. After washing, free eIF4E was released from GST by thrombin (Amersham Biosciences) digestion and further purified by gel filtration. The eIF4E preparation was quantified by Bradford protein assay.

RNA Structure Probing and Footprinting

PEMV PTE RNA element for structure probing and footprinting was prepared as described (Wang et al., 2009). PMV, CMMV, TPAV, and CarMV PTE RNAs in context of the universal cassette for SHAPE were in vitro transcribed from SmaI linearized constructs using MEGAshortscript. Solution structure probing was essentially as described previously (Wang et al., 2009). RNA (500 ng per reaction) was denatured at 94°C for 1 min then quickly chilled on ice for 2 min. The RNA was then renatured by incubation at room temperature for 30 min in 45 μl of SHAPE buffer. 5 μl of 1-methyl-7-nitroisatoic anhydride (1M7), prepared according Mortimer and Weeks (2007), was added to the renatured RNA samples and incubated at room temperature for 2 min followed by ethanol precipitation with addition of sodium acetate and yeast tRNA.

(D) Concentration of eIF4E added to PEMV2 PTE (μM): 0 (lanes 0), 0.1 (lanes 1), 0.2 (lanes 2), 0.8 (lanes 3), 2.0 (lanes 4). A, G, and T indicate dideoxy sequencing ladders. Positions of selected G nucleotides or the G domain (G), C domain (C), Loop I (LI), Loop II (LII), Helix 3 (H3), Helix 2 (H2) or Stem 1 (S1) are indicated beside gels.

(E) Secondary structure of PEMV2 PTE labeled as in (B).

(F) Predicted 3D structure of PEMV2 PTE shaded as in (C).

For footprinting, wheat eIF4E was mixed into the renatured RNA, as described above. The reaction was incubated at room temperature for 10 min to allow equilibration of protein-RNA interaction. Chemical probing of RNA-protein complex was performed by addition of 1/10 (v/v) 1M7 to the reaction and incubated at room temperature for 2 min. For enzymatic footprinting of the complex, 2 μg of yeast tRNA was added to the equilibrated reaction before addition of 0.2 U of RNase T1 (Ambion) or 0.03 U RNase V1 (Ambion), which was prepared in SHAPE buffer. The reaction was incubated at room temperature for 10 min. All reactions were stopped by addition of 50 μl of 0.6 M NaAc followed by phenol-chloroform extraction and ethanol-precipitation. Sites of modification or cutting were revealed by primer extension, urea polyacrylamide gel electrophoresis as describe previously (Wang et al., 2009). Bands were quantitated using ImageQuant software (Table S1 and Table S3).

RNA Modeling

2D Modeling

The secondary structures of the PTE elements have been determined using the MC-Fold computer program (Parisien and Major, 2008), which takes into account the energetic contribution of noncanonical base pairs, and also provides for a list of suboptimal folds. The SHAPE reactivity data provided "don't pair" constraints. The consensus secondary structure was built manually, by aligning key structural elements (Figure 7). The base pairs in the pseudoknot were such that the most SHAPE-reactive guanosine was left unpaired, and at least three base pairs were formed between the C- and G-rich strands.

3D Modeling

First, we used the computer program NAST (Jonikas et al., 2009) to sketch a coarse-grain 3D model from the secondary structure of PMV, including the pseudoknot. Second, we used the computer program MC-Sym (Major et al., 1991) to build all-atoms 3D models for the various PTE elements. Basic RNA architectural principles were used as guide for high-quality models, including NCM (Parisien and Major, 2008), coaxial stacking of stems (Levitt, 1969; Mathews et al., 2004; Tyagi and Mathews, 2007), bipolarity of helical axes, and coplanarity of the final assembly (Laederach et al., 2007). For each PTE we first built the two main axes H2-H3-SL1 (A1) and PK-SL2 (A2) using NCMs. A distance constraint of at most 5 Å between two nucleobase center-of-mass pseudo-atoms enforces coaxial stacking. These two nucleobases flank each coaxially stacked stem, and are the ones that are separated by the smallest number of nucleotides (usually consecutive in sequence). In PMV, the coaxial stacking between helices H2 and H3 is conveyed between nucleotides 4183 and 4184, between H3 and SL1 with 4145 and 4146, and between PK and SL2 with 4163 and 4164.

The two axes A1 and A2 were then assembled in 3D space around the C-rich domain and the one-nucleotide linker between H3 and SL2. The last step consisted of completing the G-rich domain.

Third, from the pool of 3D models for each of the PTE elements, we sought a consensus 3D structure that can be adopted by all the PTE elements. For each element, the top hundred P-Score models were inspected to build an all-against-all rmsd table. The rmsd is taken over all heavy atoms for nucleotides in H3 and PK (core), and for the closest three base pairs to the core in H2, SL1, and SL2. The goal is to assign one model to each element such that the sum of their pairwise rmsd is minimized. Because the search space (100^8 structures) is too vast to explore in its entirety, it was traversed using an iterative-deepening backtracking algorithm that makes use of a progression schedule heuristic. Fourthly, the consensus models were minimized using the Tinker molecular modeling package, version 5 (Ponder and Richards, 1987) and the Amber'99 forcefield (Wang et al., 2000).

Molecular Docking

Starting from the previously identified consensus structures for PMV and PEMV2 PTEs, we extracted from a pool of 10,000 decoys only those models that were at most 5 Å from the consensus structures. This yielded ~1000 models each for PMV and PEMV2. The reasoning behind this step is to provide MC-Sym with a conformational ensemble, typical of the deformation of an RNA structure under Brownian motion, on which to attempt docking of the eIF4E protein. The conformational ensemble was further extended through resampling via MC-Sym to include the single-stranded loop connecting the H2 helix to the G-rich domain of the pseudoknot. A total of 10,000 decoys were generated, for both PMV and PEMV2, as a representative set of that conformational ensemble. For the actual docking, we optimally superimposed the N2, N9, and O6 atoms of the m^7G nucleotide of the wheat eIF4E-GDP structure (Protein Data Bank [PDB] file 2IDV) to those corresponding to the SHAPE-hypermodifiable G because it is the most protected on binding to eIF4E. PDB file 2IDV was chosen, as eIF4E is cocrystallized with a m^7GTP, thus resolving the exact shape of the protein in the bound state, along with the position of the ligand. The transformation matrix resulting from that superposition was applied to all atoms of the protein, except for those in the m^7G, as they were discarded. The final product is a docking configuration of eIF4E with the PTE, where the corresponding G of the RNA replaces the m^7G. Subsequently, each docking configuration is assigned a score derived from all pairwise, interatomic distances. The score is increased for any pair of atoms, between the protein backbone and the RNA, whose distance is closer than 5 Å. From the 10,000 docking configurations we choose the one that features the smallest score, i.e., the least number of steric clashes. Finally, the chosen docking poses were submitted to an unrestrained energy minimization (Amber '99 force-field in a gas-phase until a gradient RMS of 5 Kcal/mol/Å using the L-BFGS algorithm, as implemented in the Tinker package).

SUPPLEMENTAL INFORMATION

Supplemental Information includes two figures and three tables and can be found with this article online at doi:10.1016/j.str.2011.03.013.

ACKNOWLEDGMENTS

The authors thank Anne Simon for informing us of PTEs in carmovirus RNAs. This work was funded by NIH grant R01 GM067104 with a supplement from the American Recovery and Reinvestment Act. This journal article of the Iowa Agriculture and Home Economics Experiment Station, Ames, IA, Project No. 3608 was also supported by Hatch Act and State of Iowa funds.

Received: January 2, 2011
Revised: March 11, 2011
Accepted: March 13, 2011
Published: June 7, 2011

REFERENCES

Ali, I.K., McKendrick, L., Morley, S.J., and Jackson, R.J. (2001). Activity of the hepatitis A virus IRES requires association between the cap-binding translation initiation factor (eIF4E) and eIF4G. J. Virol. *75*, 7854–7863.

Batten, J.S., Desvoyes, B., Yamamura, Y., and Scholthof, K.B. (2006). A translational enhancer element on the 3′-proximal end of the Panicum mosaic virus genome. FEBS Lett. *580*, 2591–2597.

Browning, K.S. (2004). Plant translation initiation factors: it is not easy to be green. Biochem. Soc. Trans. *32*, 589–591.

Carberry, S.E., Darzynkiewicz, E., and Goss, D.J. (1991). A comparison of the binding of methylated cap analogues to wheat germ protein synthesis initiation factors 4F and (iso)4F. Biochemistry *30*, 1624–1627.

Chen, J., and Kastan, M.B. (2010). 5′-3′-UTR interactions regulate p53 mRNA translation and provide a target for modulating p53 induction after DNA damage. Genes Dev. *24*, 2146–2156.

Culjkovic, B., Topisirovic, I., Skrabanek, L., Ruiz-Gutierrez, M., and Borden, K.L.B. (2006). eIF4E is a central node of an RNA regulon that governs cellular proliferation. J. Cell Biol. *175*, 415–426.

Doudna, J.A., and Sarnow, P. (2007). Translation initiation by viral internal ribosome entry sites. In Translational Control in Biology and Medicine, M.B. Mathews, N. Sonenberg, and J. Hershey, eds. (Cold Spring Harbor, NY: Cold Spring Harbor Laboratory Press).

Fabian, M.R., and White, K.A. (2004). 5′-3′ RNA-RNA interaction facilitates cap- and poly(A) tail-independent translation of tomato bushy stunt virus mRNA: a potential common mechanism for Tombusviridae. J. Biol. Chem. *279*, 28862–28872.

Gazo, B.M., Murphy, P., Gatchel, J.R., and Browning, K.S. (2004). A novel interaction of Cap-binding protein complexes eukaryotic initiation factor (eIF) 4F and eIF(iso)4F with a region in the 3′-untranslated region of satellite tobacco necrosis virus. J. Biol. Chem. *279*, 13584–13592.

Giedroc, D.P., and Cornish, P.V. (2008). Frameshifting RNA pseudoknots: Structure and mechanism. Virus Res. *139*, 193–208.

Gross, J.D., Moerke, N.J., von der Haar, T., Lugovskoy, A.A., Sachs, A.B., McCarthy, J.E., and Wagner, G. (2003). Ribosome loading onto the mRNA cap is driven by conformational coupling between eIF4G and eIF4E. Cell *115*, 739–750.

Guo, L., Allen, E., and Miller, W.A. (2001). Base-pairing between untranslated regions facilitates translation of uncapped, nonpolyadenylated viral RNA. Mol. Cell *7*, 1103–1109.

Haghighat, A., and Sonenberg, N. (1997). eIF4G dramatically enhances the binding of eIF4E to the mRNA 5′-cap structure. J. Biol. Chem. *272*, 21677–21680.

Jackson, R.J., Hellen, C.U., and Pestova, T.V. (2010). The mechanism of eukaryotic translation initiation and principles of its regulation. Nat. Rev. Mol. Cell Biol. *11*, 113–127.

Jonikas, M.A., Radmer, R.J., Laederach, A., Das, R., Pearlman, S., Herschlag, D., and Altman, R.B. (2009). Coarse-grained modeling of large RNA molecules with knowledge-based potentials and structural filters. RNA *15*, 189–199.

Koh, D.C., Liu, D.X., and Wong, S.M. (2002). A six-nucleotide segment within the 3′ untranslated region of hibiscus chlorotic ringspot virus plays an essential role in translational enhancement. J. Virol. *76*, 1144–1153.

Koh, D.C., Wong, S.M., and Liu, D.X. (2003). Synergism of the 3′-untranslated region and an internal ribosome entry site differentially enhances the translation of a plant virus coat protein. J. Biol. Chem. *278*, 20565–20573.

Laederach, A., Chan, J.M., Schwartzman, A., Willgohs, E., and Altman, R.B. (2007). Coplanar and coaxial orientations of RNA bases and helices. RNA *13*, 643–650.

Levitt, M. (1969). Detailed molecular model for transfer ribonucleic acid. Nature *224*, 759–763.

Lowman, H.B., and Draper, D.E. (1986). On the recognition of helical RNA by cobra venom V1 nuclease. J. Biol. Chem. *261*, 5396–5403.

Major, F. (2003). Building three-dimensional ribonucleic acid structures. IEEE Comput. Sci. Eng. *5*, 44–53.

Major, F., Turcotte, M., Gautheret, D., Lapalme, G., Fillion, E., and Cedergren, R. (1991). The combination of symbolic and numerical computation for three-dimensional modeling of RNA. Science *253*, 1255–1260.

Marcotrigiano, J., Gingras, A.C., Sonenberg, N., and Burley, S.K. (1997). Cocrystal structure of the messenger RNA 5′ cap-binding protein (eIF4E) bound to 7-methyl-GDP. Cell *89*, 951–961.

Martin, F., Barends, S., Jaeger, S., Schaeffer, L., Prongidi-Fix, L., and Eriani, G. (2011). Cap-assisted internal initiation of translation of histone H4. Mol. Cell *41*, 197–209.

Mathews, D.H., Disney, M.D., Childs, J.L., Schroeder, S.J., Zuker, M., and Turner, D.H. (2004). Incorporating chemical modification constraints into a dynamic programming algorithm for prediction of RNA secondary structure. Proc. Natl. Acad. Sci. USA *101*, 7287–7292.

Matsuo, H., Li, H., McGuire, A.M., Fletcher, C.M., Gingras, A.C., Sonenberg, N., and Wagner, G. (1997). Structure of translation factor eIF4E bound to m7GDP and interaction with 4E-binding protein. Nat. Struct. Biol. *4*, 717–724.

Merino, E.J., Wilkinson, K.A., Coughlan, J.L., and Weeks, K.M. (2005). RNA structure analysis at single nucleotide resolution by selective 2′-hydroxyl acylation and primer extension (SHAPE). J. Am. Chem. Soc. *127*, 4223–4231.

Miller, W.A., Wang, Z., and Treder, K. (2007). The amazing diversity of cap-independent translation elements in the 3′-untranslated regions of plant viral RNAs. Biochem. Soc. Trans. *35*, 1629–1633.

Monzingo, A.F., Dhaliwal, S., Dutt-Chaudhuri, A., Lyon, A., Sadow, J.H., Hoffman, D.W., Robertus, J.D., and Browning, K.S. (2007). The structure of eukaryotic translation initiation factor-4E from wheat reveals a novel disulfide bond. Plant Physiol. *143*, 1504–1518.

Mortimer, S.A., and Weeks, K.M. (2007). A fast-acting reagent for accurate analysis of RNA secondary and tertiary structure by SHAPE chemistry. J. Am. Chem. Soc. *129*, 4144–4145.

Nicholson, B.L., Wu, B., Chevtchenko, I., and White, K.A. (2010). Tombusvirus recruitment of host translational machinery via the 3′ UTR. RNA *16*, 1402–1419.

Niedzwiecka, A., Marcotrigiano, J., Stepinski, J., Jankowska-Anyszka, M., Wyslouch-Cieszynska, A., Dadlez, M., Gingras, A.C., Mak, P., Darzynkiewicz, E., Sonenberg, N., et al. (2002). Biophysical studies of eIF4E cap-binding protein: recognition of mRNA 5′ cap structure and synthetic fragments of eIF4G and 4E-BP1 proteins. J. Mol. Biol. *319*, 615–635.

Nieto, C., Morales, M., Orjeda, G., Clepet, C., Monfort, A., Sturbois, B., Puigdomenech, P., Pitrat, M., Caboche, M., Dogimont, C., et al. (2006). An eIF4E allele confers resistance to an uncapped and non-polyadenylated RNA virus in melon. Plant J. *48*, 452–462.

Parisien, M., and Major, F. (2008). The MC-Fold and MC-Sym pipeline infers RNA structure from sequence data. Nature *452*, 51–55.

Ponder, J.W., and Richards, F.M. (1987). An efficient newton-like method for molecular mechanics energy minimization of large molecules. J. Comput. Chem. *8*, 1016–1024.

Rakotondrafara, A.M., Polacek, C., Harris, E., and Miller, W.A. (2006). Oscillating kissing stem-loop interactions mediate 5′ scanning-dependent translation by a viral 3′-cap-independent translation element. RNA *12*, 1893–1906.

Stupina, V.A., Meskauskas, A., McCormack, J.C., Yingling, Y.G., Shapiro, B.A., Dinman, J.D., and Simon, A.E. (2008). The 3′ proximal translational enhancer of Turnip crinkle virus binds to 60S ribosomal subunits. RNA *14*, 2379–2393.

Su, L., Chen, L., Egli, M., Berger, J.M., and Rich, A. (1999). Minor groove RNA triplex in the crystal structure of a ribosomal frameshifting viral pseudoknot. Nat. Struct. Biol. *6*, 285–292.

Taufer, M., Licon, A., Araiza, R., Mireles, D., van Batenburg, F.H., Gultyaev, A.P., and Leung, M.Y. (2009). PseudoBase++: an extension of PseudoBase for easy searching, formatting and visualization of pseudoknots. Nucleic Acids Res. *37*, D127–D135.

Treder, K., Pettit Kneller, E.L., Allen, E.M., Wang, Z., Browning, K.S., and Miller, W.A. (2008). The 3′ cap-independent translation element of Barley yellow dwarf virus binds eIF4F via the eIF4G subunit to initiate translation. RNA *14*, 134–147.

Truniger, V., Nieto, C., Gonzalez-Ibeas, D., and Aranda, M. (2008). Mechanism of plant eIF4E-mediated resistance against a Carmovirus (Tombusviridae): cap-independent translation of a viral RNA controlled in cis by an (a)virulence determinant. Plant J. *56*, 716–727.

Tyagi, R., and Mathews, D.H. (2007). Predicting helical coaxial stacking in RNA multibranch loops. RNA *13*, 939–951.

von der Haar, T., Gross, J.D., Wagner, G., and McCarthy, J.E. (2004). The mRNA cap-binding protein eIF4E in post-transcriptional gene expression. Nat. Struct. Mol. Biol. *11*, 503–511.

Wang, J., Cieplak, P., and Kollman, P.A. (2000). How well does a restrained electrostatic potential (RESP) model perform in calculating conformational energies of organic and biological molecules? J. Comput. Chem. *21*, 1049–1074.

Wang, Z., Treder, K., and Miller, W.A. (2009). Structure of a viral cap-independent translation element that functions via high affinity binding to the eIF4E subunit of eIF4F. J. Biol. Chem. *284*, 14189–14202.

Wang, Z., Kraft, J.J., Huim, A., and Miller, W.A. (2010). Structural plasticity of Barley yellow dwarf virus-like cap-independent translation elements in four genera of plant viral RNAs. Virology *402*, 177–186.

Wells, S.E., Hillner, P.E., Vale, R.D., and Sachs, A.B. (1998). Circularization of mRNA by eukaryotic translation initiation factors. Mol. Cell *2*, 135–140.

Wilkinson, K.A., Merino, E.J., and Weeks, K.M. (2005). RNA SHAPE chemistry reveals nonhierarchical interactions dominate equilibrium structural transitions in tRNA(Asp) transcripts. J. Am. Chem. Soc. *127*, 4659–4667.

Ziegler, A., Cowan, G., and Torrance, L. (2009). Comparative sequence analysis and serological and infectivity studies indicate that cocksfoot mild mosaic virus is a member of the genus Panicovirus. Arch. Virol. *154*, 1545–1549.

Zuker, M. (2003). Mfold web server for nucleic acid folding and hybridization prediction. Nucleic Acids Res. *31*, 3406–3415.

Zuo, X., Wang, J., Yu, P., Eyler, D., Xu, H., Starich, M.R., Tiede, D.M., Simon, A.E., Kasprzak, W., Schwieters, C.D., et al. (2010). Solution structure of the cap-independent translational enhancer and ribosome-binding element in the 3′ UTR of turnip crinkle virus. Proc. Natl. Acad. Sci. USA *107*, 1385–1390.

Note Added in Proof

The structure, cap-independent translation function and long-distance base pairing to the 5′ UTR of the SCV PTE will be reported in the following publication: Chattopadhyay, M., Shi, K., Yuan, X., Simon, A.E. (2011) Long-Distance Kissing Loop Interactions between a 3′ Proximal Y-Shaped Structure and Apical Loops of 5′ Hairpins Enhance Translation of Saguaro Cactus Virus. Virology (In press).

